Quantum dynamics study of fulvene double bond photoisomerization: The role of intramolecular vibrational energy redistribution and excitation energy

Lluís Blancafort, Fabien Gatti, and Hans-Dieter Meyer

Additional information on J. Chem. Phys.

Quantum dynamics study of fulvene double bond photoisomerization: The role of intramolecular vibrational energy redistribution and excitation energy

Lluís Blancafort,[1,a)] Fabien Gatti,[2] and Hans-Dieter Meyer[3]

[1]*Institut de Química Computacional, Department de Química, Universitat de Girona, Campus de Montilivi, 17071 Girona, Spain*
[2]*CTMM, Institut Charles Gerhardt Montpellier (UMR 5253), CC 1501, Université Montpellier 2, 34095 Montpellier Cedex 05, France*
[3]*Theoretische Chemie, Ruprecht-Karls-Universität, Im Neuenheimer Feld 229, 69120 Heidelberg, Germany*

The double bond photoisomerization of fulvene has been studied with quantum dynamics calculations using the multi-configuration time-dependent Hartree method. Fulvene is a test case to develop optical control strategies based on the knowledge of the excited state decay mechanism. The decay takes place on a time scale of several hundred femtoseconds, and the potential energy surface is centered around a conical intersection seam between the ground and excited state. The competition between unreactive decay and photoisomerization depends on the region of the seam accessed during the decay. The dynamics are carried out on a four-dimensional model surface, parametrized from complete active space self-consistent field calculations, that captures the main features of the seam (energy and locus of the seam and associated branching space vectors). Wave packet propagations initiated by single laser pulses of 5–25 fs duration and 1.85–4 eV excitation energy show the principal characteristics of the first 150 fs of the photodynamics. Initially, the excitation energy is transferred to a bond stretching mode that leads the wave packet to the seam, inducing the regeneration of the reactant. The photoisomerization starts after the vibrational energy has flowed from the bond stretching to the torsional mode. In our propagations, intramolecular energy redistribution (IVR) is accelerated for higher excess energies along the bond stretch mode. Thus, the competition between unreactive decay and isomerization depends on the rate of IVR between the bond stretch and torsion coordinates, which in turn depends on the excitation energy. These results set the ground for the development of future optical control strategies. © *2011 American Institute of Physics*. [doi:10.1063/1.3643767]

I. INTRODUCTION

One of the main challenges for chemists today is to use laser pulses to control reactions.[1] In some cases, mode selectivity has provided a way to guide these processes successfully, so that desired products are obtained preferentially. This field also offers new possibilities for the understanding of fundamental phenomena involving the conversion of light into mechanical motion such as the elementary steps of vision, photosynthesis, protein dynamics, and electron and proton transport in DNA.[1] However, the control of chemical reactions by laser pulses cannot be done without knowing and controlling the time scales and the properties of the intramolecular energy redistribution in molecules. Much theoretical effort has thus been directed toward the investigation of the underlying quantum dynamics.

In former papers (see Chapter 21 in Ref. 2 for a review), some of us have demonstrated that the multi-configuration time dependent Hartree (MCTDH) algorithm[3,4] is an efficient tool to investigate the energy redistribution in molecules in their electronic ground state after excitation by a laser pulse. We have, for instance, studied the *cis-trans* isomerization[5–7] of HONO or the inversion[8] of NHD_2 in full dimensionality.

In these works, the processes were guided through quantum mechanical effects, namely, tunneling, but the molecules were considered in their electronic ground state only (Born-Oppenheimer approximation). In contrast to this, photochemistry is often governed by strong non-Born-Oppenheimer couplings between the electronic structure and the nuclear dynamics, at regions of conical intersection. In general, an intersection enables fast decay to the ground state, and it acts as a bifurcation between different reaction paths that can lead to the initial reactant and a photoproduct, or to different photoproducts.[9–13] It is therefore amenable to optical control, at least in principle. A further possibility of control is given by the extended nature of the conical intersection seam.[14] Several potential energy surface studies on different molecules have shown that the seam of intersection can be composed of different segments, each one associated to reaction channels leading to different species.[15–19] In this case, the outcome of the excitation process depends on the seam segment encountered in the decay to the lower state. Therefore, the present work can be seen as a first step to extend our studies of the intramolecular energy redistribution with the MCTDH approach to a reaction where the key step is the passage through a conical intersection seam. In such a challenging scenario, our mechanistic knowledge of the reaction shall provide the guiding principles for future control strategies.

a)Electronic mail: lluis.blancafort@udg.edu.

135, 134303-1

The idea of optical control at a seam has been tested before in direct dynamics studies, both at the quantum and mixed quantum classical dynamics level. In these studies the wave packet propagations or mixed quantum classical trajectories are guided to different seam segments varying the initial position or momentum.[15,16,18,20] While this scheme provides a proof of principle of this type of control, our aim here is to implement it in a quantum dynamics formalism that allows to include explicitly the laser pulse required for a realistic simulation. In particular, in this paper we derive a suitable four-dimensional model to simulate the photoisomerization of a polyatomic molecule, fulvene, and carry out propagations with different laser pulses. These propagations prove the suitability of the model surface for the dynamics, and provide a first approach to understand the factors on which the photoisomerization depends.

Our idea of control is illustrated in Figure 1 for the case of fulvene, an unsaturated, non-fluorescent hydrocarbon with a delocalized π system. The photophysics of fulvene is characterized by a broad, weak, and diffuse S_1 absorption band, corresponding to a valence excited state of B_2 symmetry.[21–23] The shape of the band is thought to arise from large geometry changes that occur immediately after the excitation, and the absence of fluorescence suggests the presence of a conical intersection seam between the ground and lowest excited state that enables the fast decay of the excited species. These experimental features have been explained by *ab initio* calculations that show that there is an energetically accessible S_1/S_0 seam of conical intersection.[10,24] The potential energy surface along the two relevant coordinates, a totally symmetric bond alternating mode and the CH_2 torsional mode, is sketched in Figure 1. Along the torsional coordinate there are two symmetric minima corresponding to two chemically equivale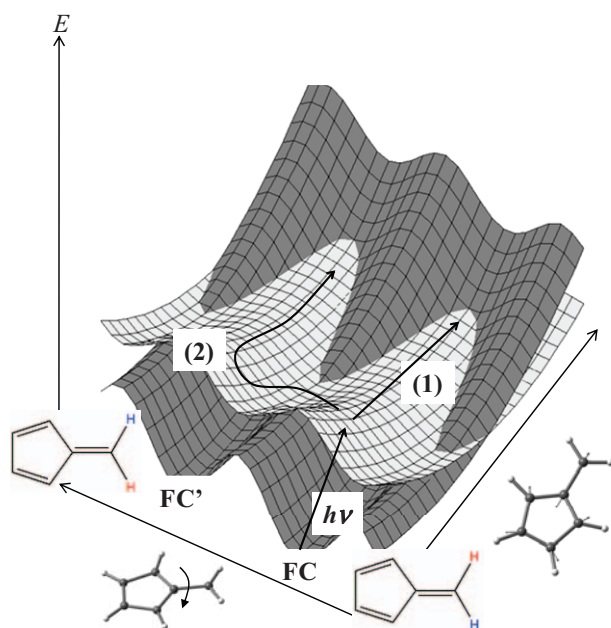nt species (coded by the different color of the methylene hydrogen atoms in Figure 1). The two isomers are connected by a double bond isomerization. They are labeled **FC**, which stands for Franck-Condon geometry, and **FC′**. Every point on the seam plotted in Figure 1 is a conical intersection if another coordinate (the interstate coupling coordinate, see below) is taken into account. When a wave packet is promoted to the electronically excited state from one of the ground state minima, **FC**, there are two possibilities: (1) decay in the region of the seam close to **FC**, reached along the bond alternating coordinate, which will regenerate the reactant, or (2) double bond twisting before the decay, which will allow for the decay at the seam segment close to **FC′** and induce the double bond isomerization. Based on this picture, fulvene is a good system to test optical control strategies which aim to govern the reactivity by controlling the segment of the seam where decay of the wave packet takes place.

The photodynamics of fulvene has been the subject of several previous theoretical dynamics studies. The decay along the seam was studied in an early example with mixed quantum classical dynamics (classical propagation of the nuclei combined with a trajectory surface hopping algorithm) which showed that different trajectories decay to the ground state at different points on the seam.[10] Recently there have been several quantum dynamics studies on two- and three-dimensional surfaces with the goal of separating nuclear spin isomers.[25–27] In one of these studies, it was found that the occurrence of the isomerization depended on the shape of the excitation laser pulse.[26] The control of the photoisomerization of fulvene has also been addressed recently in a direct full dimensional variational multi-configurational Gaussian (vMCG) dynamics study.[20] In this case, the isomerization depended on the initial momentum and position of the wave packet. In the present paper we carry out a quantum dynamics study on a four-dimensional model surface, using the MCTDH approach.[2–4,28] We use the idea of control at the conical intersection seam to guide our choice of coordinates, centering on the coordinates corresponding to seam segments of low energy. As we will show in Sec. II, a set of four coordinates provides a very good model for the potential energy surface along these segments. This happens at the expense of taking some approximations, but it is largely compensated by the good description of the surface and the relative simplicity of the potential. On this model we have carried out propagations with single laser pulses as a first attempt of a realistic simulation of the control. Initially, the vibrational energy is located on a bond stretching mode, and the photoisomerization depends on the intramolecular vibrational redistribution (IVR) to the torsional mode, which in turn depends on the energy of the excitation pulse.

FIG. 1. Potential energy surface sketch for the S_1 and S_0 states of fulvene along the torsional and symmetric bond alternation coordinates, displaying the paths for photostability (1) and photoisomerization (2).

II. ELECTRONIC STRUCTURE CALCULATIONS AND PARAMETRIZATION OF THE ELECTRONIC HAMILTONIAN

Our choice of coordinates aims to capture the lowest energy region of the seam and its most important features, including the branching space vectors, and the minimum energy path from the **FC** structure to the seam. The excited state relaxation and intersection space of fulvene have been studied
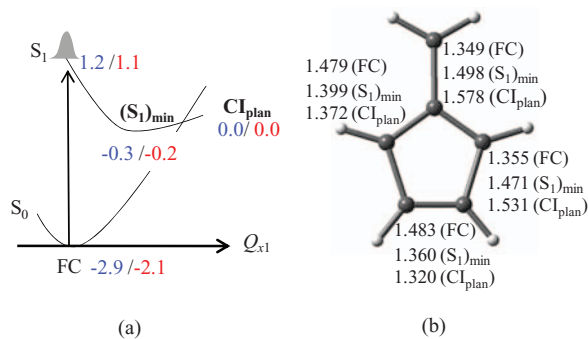
FIG. 2. (a) Potential energy profile for the initial excited state relaxation coordinate along planar structures (energies in eV with respect to S_1 energy at **FC** structure; *ab initio* data in blue and model data in red). (b) Bond lengths in Å for optimized structures along the relaxation coordinate.

in detail previously with electronic structure calculations at the complete active space self-consistent field (CASSCF) level of theory.[10,24] We base our choice on these results, which are summarized briefly. The initial part of the decay (see Figure 2) retains the planarity of the molecule and involves a bond inversion coordinate that leads to a minimum on the excited state surface, $(S_1)_{Min}$, and further to a conical intersection with the ground state, CI_{plan} (see optimized *ab initio* energies in blue in Figure 2(a) and bond lengths in Figure 2(b)). CI_{plan} belongs to an extended intersection space that contains two low energy segments along the CH_2 torsion and pyramidalization coordinates. Overall, the seam contains four relevant conical intersection stationary points (see Table I for a summary of the energies). These structures are shown in Figure 3, together with the displacements corresponding to the branching space vectors. These vectors are the gradient difference (**gd**) and interstate coupling (**ic**) vectors that lift the degeneracy at the intersection at first order (see Eq. (1)):

$$\mathbf{gd} = \nabla_{\mathbf{Q}}(E_2 - E_1), \tag{1a}$$

$$\mathbf{ic} = \langle \Phi_1 | \nabla_{\mathbf{Q}} \hat{H}_{ele} | \Phi_2 \rangle. \tag{1b}$$

TABLE I. Energies of the optimized critical points relative to CI_{plan} at the *ab initio* level (CASSCF and CASPT2) compared to the four-dimensional model Hamiltonian **W**.

Structure	E_{rel}^{CASSCF} (eV)[a]	E_{rel}^{CASPT2} (eV)[b]	E_{rel}^{model} (eV)
FC (S_0)	-2.88	-2.77	-2.11
FC (S_1)[c]	1.25	-0.97	1.12
$(S_1)_{Min}$	-0.28	-0.17	-0.19
CI_{plan}	0.00	$0.00 (0.31)^d$	0.00
CI_{perp}	-0.33	$-0.16 (0.06)^d$	-0.33
CI_{63}	-0.07	$-0.01 (0.28)^d$	-0.06
CI_{pyr}	-0.42	$-0.34 (0.20)^d$	-0.40

[a]Energies of CASSCF(6,6)/cc-pvdz optimized points using GAUSSIAN 03 (Ref. 29) (see Ref. 24 for details).
[b]Single point CASPT2(6,6)/cc-pvdz energies on CASSCF optimized structures. Energies calculated with Molcas 7.2 (Ref. 30) state averaging over the two lowest states with equal weights, a real level shift (Ref. 31) of 0.1 a.u. and an ionization potential electron affinity shift (Ref. 32) of 0.25 a.u.
[c]Experimental vertical excitation: 3.44 eV (Ref. 21).
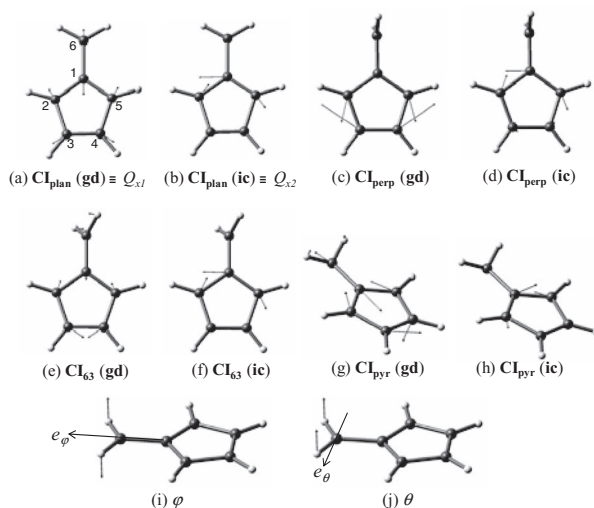[d]Average of CASPT2 S_1 and S_0 energies; S_1–S_0 energy gap in brackets.

FIG. 3. (a)–(h) Relevant conical intersection structures for fulvene, showing the mass-weighted displacements corresponding to the **gd** and **ic** vectors. (i) and (j) Torsion and pyramidalization coordinates.

In Eq. (1b), Φ_i is the adiabatic electronic wave function for state i. The four conical intersections differ in the orientation of the CH_2 group with respect to the ring: at CI_{perp}, the CH_2 group lies perpendicular to the plane (torsion angle of $90°$ around the double bond), CI_{63} has an intermediate structure between CI_{plan} and CI_{perp} (torsion angle of $63°$), and CI_{pyr} has the CH_2 group pyramidalized with respect to the plane. From the point of view of energy, the energy of the seam with respect to CI_{plan} decreases along the torsion and pyramidalization coordinates. CI_{63} coincides to a very good approximation with the global energy minimum of the seam, labeled CI_{min} in Ref. 24, which is less than 1 meV lower in energy than CI_{63}. As we discuss in this section, this space of intersection can be described by four coordinates (Figure 3): a totally symmetric and a non-totally symmetric bond stretch coordinate (Q_{x_1} and Q_{x_2}, respectively), which correspond to the branching space vectors at CI_{plan} (Figures 3(a) and 3(b)), and the torsion angle φ and the pyramidalization angle θ (Figures 3(i) and 3(j)). Q_{x_1} and Q_{x_2} are treated as mass-weighted Cartesian displacements, while φ and θ are curvilinear coordinates corresponding to rotation of the rigid CH_2 group around the axes e_φ and e_θ in Figures 3(i) and 3(j), respectively (e_φ is the axis through the C_1–C_6 bond, while e_θ is the axis through C_6 in the plane of the ring, perpendicular to e_φ).

From the point of view of the electronic structure, the seam involves three electronic configurations, as shown by the analysis of the CASSCF wave function summarized in Figure 4 (orbital correlation diagram and configurations of the three lowest states along φ). At planar structures of C_{2v} symmetry, the ground state has A_1 and the excited state B_2 symmetry. Along the torsional coordinate the symmetry is lowered to A and B, respectively. At $\varphi = 90°$, the structure has C_{2v} symmetry, and the two lowest states have A_2 and B_1 symmetry. The $1A_2$ state at perpendicular geometries correlates diabatically with S_2 at the planar structures, while the ground state at planar structures correlates with S_2 at the structure with $\varphi = 90°$. In principle such a situation could be described

as a three state problem where the two states of A symmetry are highly coupled along the torsional coordinate. However, the two lowest states are separated from S_2 by at least 1.9 eV at the CASSCF level, and a two-state treatment is satisfactory for the present dynamics.

For the dynamics, the two-state potential energy matrix **W** was parametrized with respect to CASSCF(6,6)/cc-pvdz calculations over two states, state averaging with equal weights. This level of theory only gives non-dynamic electronic correlation, but complete active space second order perturbation (CASPT2) calculations on the critical points indicate that the effect of dynamic correlation is small (see Table I), with a maximum deviation of 0.3 eV between the CASSCF and CASPT2 relative energies. The CASPT2 energy gaps at the CASSCF conical intersection structures are

also smaller than 0.3 eV, and in all cases we have located the CASPT2 intersections in the vicinity of the CASSCF optimized structures. Therefore, the CASSCF level of theory is satisfactory for our purpose.

The potential energy matrix **W** along the four-dimensional vector of coordinates $\mathbf{Q} = \{Q_{x_1}, Q_{x_2}, \varphi, \theta\}$ is given by a modified version of the diabatic vibronic coupling (2×2) Hamiltonian,[33] where the diabatic basis is used to avoid singularities at the points of conical intersection. The electronic Hamiltonian **W** has the following form:

$$V_{1,2} \equiv \mathbf{W} = \begin{pmatrix} W_1 & W_{12} \\ W_{12} & W_2 \end{pmatrix} = W^0 \mathbf{I} + \begin{pmatrix} W_{11} & W_{12} \\ W_{12} & W_{22} \end{pmatrix}, \quad (2a)$$

$$\begin{aligned} W^0 = {} & (\lambda_0 + \lambda_{x_1,\varphi} \sin^2(\varphi))Q_{x_1} + \frac{1}{2}(\omega_{x_1} + \omega_{x_1,\varphi} \sin^2(\varphi))Q_{x_1}^2 + \frac{1}{2}\omega_\varphi \sin^2(\varphi) \\ & + \frac{1}{2}\varsigma_\varphi \sin^4(\varphi) + \left(\frac{1}{2}\omega_\theta + \frac{1}{2}\omega_{x_1,\theta}Q_{x_1} + \frac{1}{2}\omega_{\varphi,\theta} \sin^2(\varphi)\right)\theta^2 \\ & + \left(\frac{1}{2}\varsigma_\theta + \frac{1}{2}\varsigma_{x_1,\theta}Q_{x_1} + \frac{1}{2}\varsigma_{\varphi,\theta} \sin^2(\varphi)\right)\theta^4 + \frac{1}{2}\omega_{x_2}Q_{x_2}^2, \end{aligned} \quad (2b)$$

$$W_{11} = -\frac{1}{2}\begin{bmatrix} [\delta\kappa + \delta\kappa_{x_1,\varphi} \sin^2(\varphi)]Q_{x_1} + \frac{1}{2}[\delta\gamma_{x_1} + \delta\gamma_{x_1,\varphi} \sin^2(\varphi)]Q_{x_1}^2 + \frac{1}{2}\delta\gamma_\varphi \sin^2(\varphi) \\ + \frac{1}{2}\chi_\varphi \sin^4(\varphi) + \left(\frac{1}{2}\delta\gamma_\theta + \frac{1}{2}\delta\gamma_{x_1,\theta}Q_{x_1} + \frac{1}{2}\delta\gamma_{\varphi,\theta} \sin^2(\varphi)\right)\theta^2 \\ + \left(\frac{1}{2}\chi_\theta + \frac{1}{2}\chi_{x_1,\theta}Q_{x_1} + \frac{1}{2}\chi_{\varphi,\theta} \sin^2(\varphi)\right)\theta^4 + \frac{1}{2}\delta\gamma_{x_2}Q_{x_2}^2 \end{bmatrix}, \quad (2c)$$

$$W_{22} = -W_{11}, \quad (2d)$$

$$W_{12} = \left(\kappa_{\varphi,\theta}^{AB} \sin^2(\varphi) + \kappa_{\varphi,\theta2}^{AB} \sin^4(\varphi)\right)\theta + \kappa_{x_2}^{AB}Q_{x_2}. \quad (2e)$$

In Eq. (2a), $V_{1,2}$ are the adiabatic state energies. For the diagonal elements of **W**, the W^0 expansion (Eq. (2b)) is the average energy between the diabatic states, and W_{11} is half the energy difference. In our choice of the

terms contained in W^0 and W_{11} we have aimed at obtaining a reasonably accurate fit with the smallest possible number of terms. Thus, the W_0 expansion contains a linear and a quadratic term along Q_{x_1} (λ_0 and ω_{x_1} parameters), a quadratic term along Q_{x_2} (parameter ω_{x_2}), and a quadratic and a quartic term along θ (parameters ω_θ and ζ_θ). The torsional coordinate φ is described with the $\sin^2$ and $\sin^4$ functions (ω_φ and ζ_φ parameters, respectively) because the potential is periodic in π along φ. W^0 also includes six bimodal terms between the different coordinates, which are the most relevant ones to obtain a good fitting of the surface. The W_{11} expansion has an analogous structure to W^0. Turning to the coupling element W_{12}, we include a single linear coupling term along Q_{x_2} ($\kappa_{x_2}^{AB}$) because the length and direction of the **ic** vector is approximately constant along the surface (see below for details). Two additional terms are included in W_{12} to describe the bimodal coupling along θ and φ, since its value changes significantly in the space spanned by the two angles.

Before the details of the parametrization are discussed, a brief consideration on symmetry is helpful to understand how the elements of the diabatic potential energy matrix are approximated. At planar configurations of C_{2v} symmetry, the four coordinates Q_{x_1}, Q_{x_2}, φ, and θ have a_1, b_2, a_2, and b_1 symmetry, respectively. The $1A_1$ and $1B_2$ states provide a natural choice for the diabatic states, and the diagonal
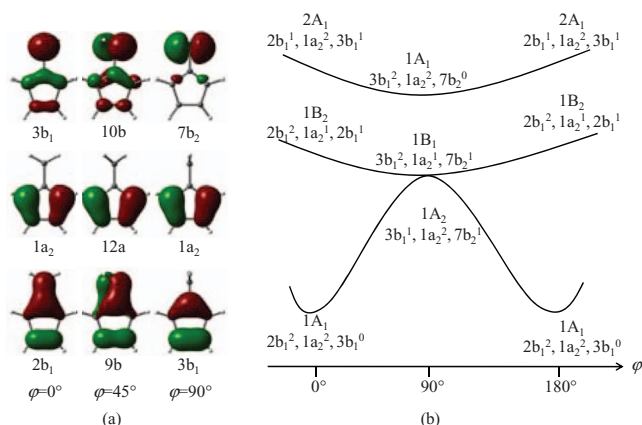

FIG. 4. Electronic wave function analysis along the torsional coordinate. (a) Correlating orbitals involved in the excitations. (b) Electronic states and dominant configurations.

elements of $\mathbf{W}$ coincide with the adiabatic energies for cuts of the surface where $Q_{x_2} = 0$ and $\varphi\theta = 0$. Therefore, all parameters can be fitted directly to the *ab initio* data, except those that involve terms that depend on Q_{x_2} or couple φ and θ. For the latter parameters we use the regularized diabatic states approach,[34] where the couplings are expressed through off-diagonal potential terms of the diabatic Hamiltonian (W_{12}). These terms are obtained using the unitary transformation that converts the adiabatic *ab initio* energies into the elements of $\mathbf{W}$, as we explain below.

The origin of $\mathbf{W}$ lies at $\mathbf{CI_{plan}}$, of C_{2v} symmetry, and the totally symmetric stretching coordinate Q_{x_1} corresponds to the **gd** vector at the intersection (Eq. (1a)). In our model, Q_{x_1} also connects $\mathbf{CI_{plan}}$ with the **FC** structure, since it is the only coordinate of a_1 symmetry. The energy profile along this coordinate (surface cut for $(Q_{x_2}, \varphi, \theta) = (0,0,0)$) in the model is compared with the *ab initio* energies of optimized points in Figure 2(a) (model energies in red and *ab initio* data in blue; see also the data in Table I). There is good agreement between the CASSCF data and the model for the energy of $\mathbf{(S_1)_{Min}}$ and the excited state energy at the **FC** structure, but there is a deviation of almost 1 eV for the vertical excitation energy (4.1 eV at the *ab initio* level and 3.2 eV in the model). This discrepancy is not due to the fit, but to the fact that we use the **gd** vector at $\mathbf{CI_{plan}}$ as the totally symmetric coordinate to obtain a good description of the seam. A different coordinate might be chosen to improve the agreement between the relative energies, but this would cause a worse description of the seam. Therefore, inclusion of more totally symmetric modes would be the best way to improve the vertical excitation energy of the model. However, the early stages of the dynamics depend mainly on the S_1 surface, which is well reproduced by the present model.

The Q_{x_1} and φ coordinates are highly coupled because of the high coupling between the S_0 and S_2 electronic states along the torsional mode (S_2 is not included in the Hamiltonian). To obtain the parameters for terms of Q_{x_1} and φ we have followed a two-step procedure: in the first step, the parameters for the terms that depend only on φ ($\omega_\varphi, \zeta_\varphi, \delta\gamma_\varphi, \chi_\varphi$) are fitted with respect to *ab initio* calculations for geometries in the surface cut along φ for $(Q_{x_1}, Q_{x_2}, \theta) = (0,0,0)$. The parameters that couple Q_{x_1} and φ ($\omega_{x_1,\varphi}, \zeta_{x_1,\varphi}, \delta\gamma_{x_1,\varphi}, \chi_{x_1,\varphi}$) are then fitted to *ab initio* calculations subject to the constrain that the energy of $\mathbf{CI_{perp}}$ relative to $\mathbf{CI_{plan}}$ and the second derivatives of the S_0 and S_1 energies at $\mathbf{CI_{perp}}$ match the *ab initio* values. The resulting surface cut in the (Q_{x_1}, φ) plane for $(Q_{x_2}, \theta) = (0,0)$ is shown in Figure 5. The root mean square error (RMSE) for this surface cut is 0.16 eV and 0.18 eV for V_1 and V_2, respectively (parametrization based on 102 *ab initio* points). The agreement between the model and the *ab initio* data is further assessed in Figure 6. In Figure 6(a) we compare the energy of the model seam along the torsion coordinate with the *ab initio* data, and in Figure 6(b) we compare the locus of the model seam in the (Q_{x_1}, φ) plane (surface cut for $(Q_{x_2}, \theta) = (0,0)$) with the *ab initio* data. In both cases there is excellent agreement between the *ab initio* data (filled diamonds) and the model (continuous line). The agreement is confirmed by comparing the relative energies of $\mathbf{CI_{plan}}$, $\mathbf{CI_{perp}}$, and $\mathbf{CI_{63}}$, optimized at the CASSCF level, with the

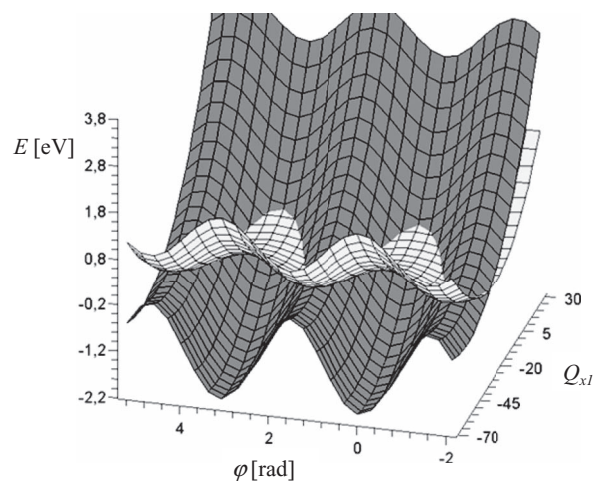FIG. 5. Plot of the model surfaces in the (Q_{x_1}, φ) plane (cuts for $(Q_{x_2}, \theta) = (0,0)$). Dark surface: W_{11}; light surface: W_{22}.

energies of the stationary points of the model (see Table I). For the terms in θ, the parameters of W^0 are obtained fitting the model to the average of the adiabatic energies. Following the regularized diabatic states approach, the parameters of W_{11} and W_{12} are fitted to the *ab initio* data using the equality:

$$\Delta V^2 = 4W_{12}^2 + (W_{22} - W_{11})^2. \quad (3)$$

Overall, the parameters corresponding to θ have been fitted to 82 *ab initio* points, with RMSE of 0.16 eV and 0.15 eV for V_1 and V_2, respectively. The parametrization provides a good description of the seam segment along the pyramidalization mode, and the relative energy of $\mathbf{CI_{pyr}}$ is well reproduced by the model (see Table I).
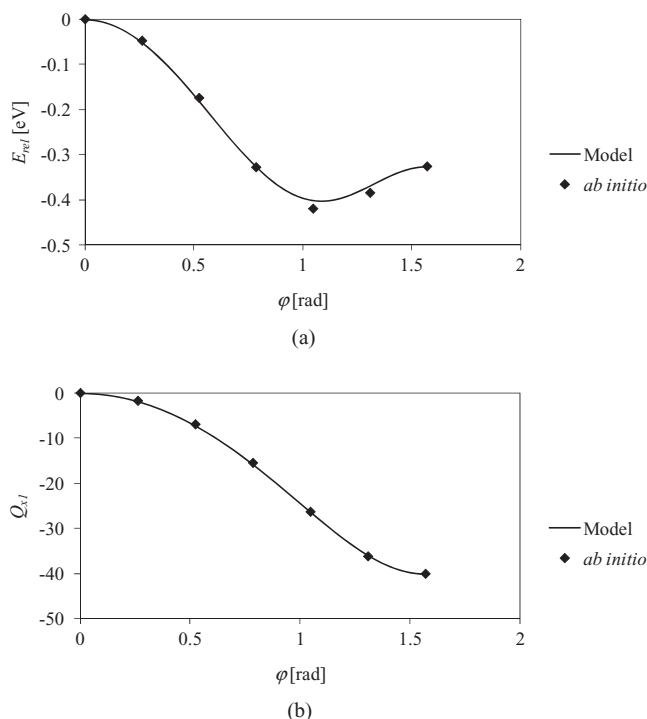

FIG. 6. Seam energy and locus of the seam in the (Q_{x_1}, φ) plane (a and b, respectively; cuts for $(Q_{x_2}, \theta) = (0,0)$), comparing the model (continuous line) with the *ab initio* data (full diamonds).

TABLE II. Summary of propagation results.

Pulse duration τ (fs)	Excitation energy $\hbar\omega$ (eV)	Electric field strength E_0 (a.u.)	Maximal V_2 population P_{max}^2	Final V_2 population P_f^2	Final W_{11} product population $p_{pr,f}^1$	Time for IVR from Q_{x_1} to φ, τ_{IVR} (fs)
5	2	1.5×10^{-1}	0.17	0.02	0.03	72
5	2.5	1.0×10^{-1}	0.37	0.05	0.12	40
5	3	7.5×10^{-2}	0.39	0.07	0.15	38
5	3.5	7.5×10^{-2}	0.34	0.07	0.14	36
5	4	1.0×10^{-1}	0.30	0.07	0.12	36
25	1.85	1.2×10^{-1}	0.12	0.01	0.01	132
25	1.9	1.2×10^{-1}	0.20	0.02	0.02	124
25	2	1.2×10^{-1}	0.38	0.04	0.04	60
25	2.5	5.0×10^{-2}	0.27	0.06	0.12	54
25	3	3.5×10^{-2}	0.31	0.10	0.20	46
25	3.5	3.5×10^{-2}	0.25	0.09	0.17	44
25	4	7.5×10^{-2}	0.24	0.10	0.16	42

Finally, for Q_{x_2} the parameter $\kappa_{Q_{x_2}}^{AB}$ is the length of **ic** at **CI**$_{\text{plan}}$ (see Eq. (1b)). Similarly, the parameters ω_{x_2} and $\delta\gamma_{x_2}$ are obtained from the curvatures of the adiabatic states at **CI**$_{\text{plan}}$.

In addition to the energy and locus of the conical intersection seam segments, the model also describes correctly the branching space along the seam. First, analysis of the conical intersection stationary points shows that the interstate coupling vector **ic** is similar in length and direction for all critical points on the seam (see Figures 3(b), 3(d), 3(f), and 3(h)), i.e., Q_{x_2} provides a good approximation to the interstate coupling vector **ic** along the seam segments included in the model. The case of the gradient difference vector **gd** is more complicated, since this vector changes its direction along the seam.[14] In general, the seam segments lie along combinations of two or more coordinates, and the **gd** vector is spanned by the same space. In the case of fulvene, for the segments along the rotation and pyramidalization coordinates the seam coordinate is a combination of Q_{x_1} and φ, and Q_{x_1} and θ, respectively, and **gd** along each segment should be spanned by the same coordinate pair. Our model agrees with this analysis. Thus, according to Eq. (1), **gd** in the (Q_{x_1},φ) plane (surface cut for (Q_{x_2},θ) = (0,0)) is a linear combination of the vectors that span the plane, $\hat{Q}_{x_1}$ and $\hat{\varphi}$:

$$\left. \frac{\partial(V_2 - V_1)}{\partial \mathbf{Q}} \right|_{Q_{x_2}=0, \theta=0}$$

$$= [\delta\kappa + \delta\kappa_{x_1,\varphi} \sin^2(\varphi) + (\delta\gamma_{x_1} + \delta\gamma_{x_1,\varphi} \sin^2(\varphi))Q_{x_1}]\hat{Q}_{x_1}$$

$$+ \left[(2\delta\kappa_{x_1,\varphi} Q_{x_1} + \delta\gamma_{x_1,\varphi} Q_{x_1}^2 + \delta\gamma_\varphi) \sin(\varphi) + 2\chi_\varphi \sin^3(\varphi) \right]\hat{\varphi}.$$

$$(4)$$

A similar expression can be derived for **gd** in the (Q_{x_1},θ) plane (surface cut for (Q_{x_2},φ) = (0,0)):

$$\left. \frac{\partial(V_2 - V_1)}{\partial \mathbf{Q}} \right|_{Q_{x_2}=0, \varphi=0}$$

$$= \left[\delta\kappa + \delta\gamma_{x_1} Q_{x_1} + \frac{1}{2}\delta\gamma_{x_1,\theta}\theta^2 + \frac{1}{2}\chi_{x_1,\theta}\theta^4 \right]\hat{Q}_{x_1}$$

$$+ [(\delta\gamma_\theta + \delta\gamma_{x_1,\theta} Q_{x_1})\theta + 2(\chi_\theta + \chi_{x_1,\theta} Q_{x_1})\theta^3]\hat{\theta}. \quad (5)$$

These expressions are consistent with the *ab initio* results. For example, **gd** at **CI**$_{63}$, which lies in the (Q_{x_1},φ) plane, has a component along the CH$_2$ torsion angle φ (Figure 3(e)). Similarly, **gd** at **CI**$_{\text{pyr}}$ has a component along the CH$_2$ pyramidalization angle θ (Figure 3(g)).

To summarize, the parameters of **W** have been fit to a total of 233 points, with RMSE values of 0.15 eV and 0.16 eV for V_1 and V_2, respectively. More importantly, the set of four coordinates $\{Q_{x_1}, Q_{x_2}, \varphi, \theta\}$ provides a good description of the energies of the critical points, including the relaxation path on S$_1$ along Q_{x_1}, and the seam segments along φ and θ. In future work, the four-dimensional model could be improved by including more terms in the expansion of **W** (Eq. (2)). However, it seems more important to include more coordinates to improve the agreement between the *ab initio* data and the model, in particular the vertical excitation energy (see Figure 2).

III. MCTDH PROPAGATION DETAILS

The propagations are carried out integrating the time dependent Schrödinger equation of the form:

$$i\hbar \frac{\partial}{\partial t} \begin{pmatrix} |\Psi_1^d(t)\rangle \\ |\Psi_2^d(t)\rangle \end{pmatrix} = (\mathbf{W} + \mathbf{T} + \mathbf{H}_{int}) \begin{pmatrix} |\Psi_1^d(t)\rangle \\ |\Psi_2^d(t)\rangle \end{pmatrix}, \quad (6)$$

where **W** is the potential energy matrix described in Sec. II. **T** is approximated by a diagonal kinetic energy operator (KEO) with terms:

$$\hat{T} = \sum_{i=1,2} \hat{T}_{Q_{x_i}} + \hat{T}_\varphi + \hat{T}_\theta, \quad (7a)$$

$$\hat{T}_{Q_{x_i}} = -\frac{1}{2\mu_i} \frac{\partial^2}{\partial Q_{x_i}^2} \quad (i=1,2), \quad (7b)$$

$$\hat{T}_\xi = -\frac{1}{2I_\xi} \frac{\partial^2}{\partial \xi^2} \quad (\xi = \varphi, \theta), \quad (7c)$$

where μ_i is the reduced mass of Q_{x_i} and I_ξ is the moment of inertia corresponding to coordinate ξ. The KEO given above is obviously approximate. First, θ involves a displacement of

the center of mass (see Figure 3(j)) which is neglected in this approximation, but the effect is small. We have also neglected the coupling between the normal coordinates and the two angles. The derivation of this coupling would lead to a very involved expression of the KEO, in a form which would not be apt for an optimal use of MCTDH, i.e., a direct product form in terms of the coordinates. Moreover, we assume that the omission of the coupling leads to an error that is smaller than the error due to the fact that we take into account only four degrees of freedom in the potential. In fact, using a mixture of normal and curvilinear coordinates along with the above approximate expression of the KEO is the price to pay for a correct description of the reaction path and the branching space with only four degrees of freedom and a simple expression of the KEO. A further improvement of our approach would be to reformulate the description of the system in terms of the so-called "polyspherical coordinates".[35] A rigorous derivation of the corresponding KEO could then be performed, and the final expression would be perfectly adapted to a direct implementation in MCTDH. However, more than four degrees of freedom would be required to describe the seam and branching space correctly.

$\mathbf{H}_{int}$ describes the interaction between the wave packet and an external electric field (laser pulse) and has the form:

$$\mathbf{H}_{int} = \begin{pmatrix} 0 & -\mu_{12}E(t) \\ -\mu_{12}E(t) & 0 \end{pmatrix}, \qquad (8)$$

where μ_{12} is the transition dipole moment between S_0 and S_1. The value of μ_{12} is estimated as 0.2222 a.u. at the CASSCF level (**FC** geometry) and is assumed to be independent of the coordinates, following the Condon approximation.

The dynamics were carried out with the MCTDH approach.[3,4,28] For Q_{x_1} and Q_{x_2} we used a primitive basis of 48 and 25 harmonic oscillator functions, respectively, for φ a fast fourier transform collocation of 128 functions, and for θ a primitive basis of 25 sine functions. For the single particle basis, we have used a combined mode for Q_{x_1} and φ (50 single particle functions (SPFs) per diabatic state), as explained in Section 4.5 of Ref. 4, and 25 and 20 SPF per state for Q_{x_2} and θ, respectively (i.e., a total of 25 000 configurations per state). The propagations, which were run over 150 fs, are well converged with respect to the number of SPF, since in all runs the maxima over time of the lowest natural weight for all modes did not exceed 0.001. Regarding the propagation length, test runs show that phase space saturation starts to appear at times longer than 150 fs. Inclusion of more degrees of freedom in our model seems to be necessary to avoid this problem and propagate for longer times.

The propagations were initiated exciting the wave packet from the vibrational ground state to the electronic excited state with a single laser pulse of the form:

$$E(t) = E_0 \cos(\omega t) \sin^2\left(\frac{\pi}{\tau}t\right), \qquad (9)$$

where E_0 is the intensity of the pulse, $\hbar\omega$ is the excitation energy, and τ is the pulse duration (the pulse was set to zero outside the $[0,\tau]$ interval). We ran two sets of calculations with a pulse duration of 5 fs and 25 fs, varying the excitation energy from 1.85 eV (0–0 transition) to 4.0 eV. For every

propagation E_0 was tuned such that the maximum population of V_2 (adiabatic excited state) lied approximately between 0.2 and 0.4. The resulting intensities lie between 0.03 and 0.15 a.u., which corresponds to 6×10^{13}–2×10^{15} W cm^{-2}, approximately. These intensities may not be practical because they may induce Coulomb explosion, but in the present work it is preferable to use these values to get significant population transfer to the excited state and facilitate the population analysis. In future work, it should be possible to apply less intense fields and extend the length of the pulse. Longer propagations will become reliable when more degrees of freedom are included in the model, as mentioned above.

Fulvene is symmetric with respect to the torsion coordinate, which implies that the nuclear wave function should be symmetric with respect to φ.[25–27] Thus, the ground state V_1 has a double well potential along φ with a high barrier, and the vibrational ground state has two doubly degenerate, symmetry adapted solutions (the energy difference is smaller than 10^{-6} a.u.). To monitor the double bond isomerization it is more convenient to propagate a symmetry broken, localized wave packet centered around $\varphi = 0$, obtained from a linear combination of the symmetry adapted ones. In this case, we calculate the evolution of the expectation value of $\langle\varphi\rangle$ in two intervals, $\varphi \in [-\pi/2, \pi/2]$ (initial configuration) and $\varphi \in [\pi/2, 3\pi/2]$ (isomerized configuration). The expectation values were calculated for the adiabatic states following the procedure described in Ref. 36. In this procedure, the expectation values of the adiabatic state V_i can be calculated from the diabatic wave functions using Eq. (10):

$$p_{int}^i = \langle \mathbf{\Psi}^d | \mathbf{P}^{(i)} \hat{\varphi}_{step} | \mathbf{\Psi}^d \rangle. \qquad (10)$$

In Eq. (10), $\hat{\varphi}_{step}$ is a step operator for the desired interval, and $\mathbf{P}^{(i)}$ is the projection matrix in diabatic representation onto the ith adiabatic state. The matrix elements of the projection matrix are first generated on the product grid and then transformed to a product representation with the so-called *potfit* algorithm.[4,37,38] The resulting adiabatic expectation values are interpreted as populations of the reactant configuration, p_{rct}^1 and p_{rct}^2 ($\varphi \in [-\pi/2, \pi/2]$) and product populations, p_{pr}^1 and p_{pr}^2 ($\varphi \in [\pi/2, 3\pi/2]$).

IV. DYNAMICS RESULTS AND DISCUSSION

A. Vertical excitation propagation

As a first approach to the photodynamics, and for comparison with the previous quantum dynamics studies,[20,25–27] we carried out one propagation where the initial ground state wave packet is transferred to the excited state with an instantaneous vertical excitation. The results are plotted in Figures 7(a) and 7(b). These figures show the key parameters for the isomerization, the adiabatic populations of the reactant, and product configurations obtained from $\langle\varphi\rangle$. Initially the wave packet is on V_2 in the reactant configuration ($p_{rct}^2 = 1$). The propagation has two phases. During the first 30 fs, approximately, there is a substantial population transfer to V_1 (decrease of p_{rct}^2 and increase of p_{rct}^1), without appreciable torsion around the double bond (p_{pr}^1 and p_{pr}^2 stay zero). The efficient deactivation can be readily understood from the
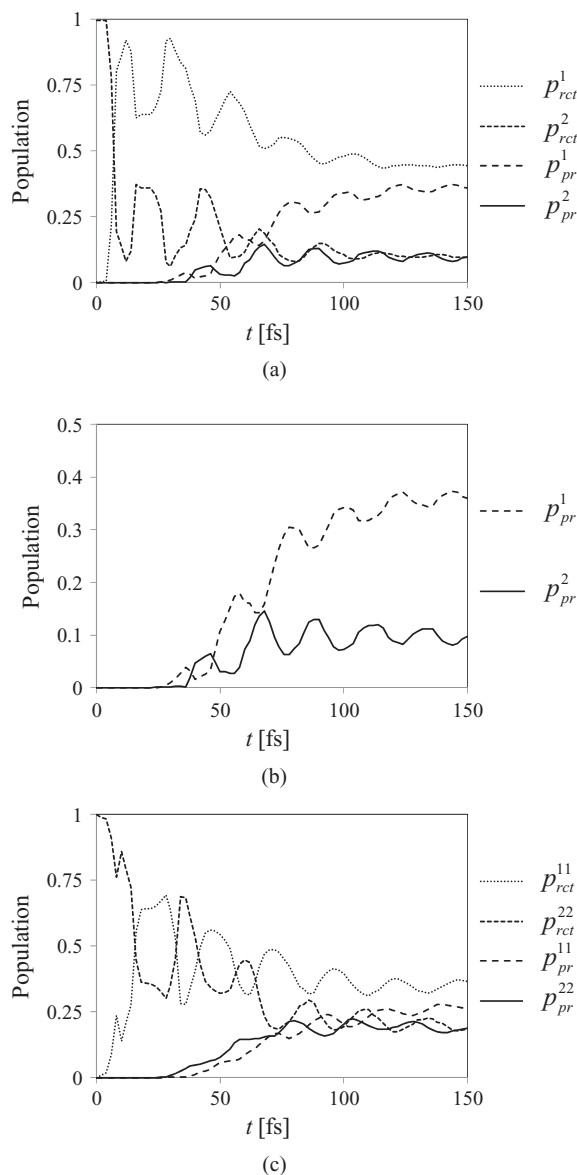
FIG. 7. (a) Reactant and product populations for the two adiabatic states after instantaneous vertical excitation. p^1_{rct} (dotted line); p^2_{rct} (short hashed line); p^1_{pr} (long hashed line); p^2_{pr} (continuous line). (b) Detailed plot of p^1_{pr} and p^2_{pr}. (c) Same as (a) for the diabatic states.

energy profile along Q_{x_1} (see Figure 2). Thus, the wave packet acquires more than 1 eV initial vibrational energy along this coordinate, and the seam of intersection is energetically accessible. Initially the decay occurs in the vicinity of **CI$_{plan}$**, since no population builds up for p^1_{pr}. The second phase starts after around 30 fs, when the double bond starts to twist (rise of p^1_{pr} and p^2_{pr}). For the initial value $\varphi = 0$ the V_2 surface has a negative curvature along φ, and the inset of the torsion gives a measure of the time that is required for IVR from Q_{x_1} to φ. The value of 30 fs determined in the present case agrees approximately with the value given in Ref. 27 for propagation on a two-dimensional surface, where the torsion of the methylene groups takes $\sim$50 fs. The part of the wave packet that spreads along φ on V_2 decays to V_1 almost instantaneously, as seen by the rise of p^1_{pr}, because the seam has a peaked topology around $\varphi = \pi/2$, i.e., all the population around that

region is funneled almost immediately from the upper to the lower state. After 150 fs, 81% of the total population has been transferred to the ground state, where the reactant and product populations are 0.45 and 0.36, respectively. Thus, there is no selectivity in favor of unreactive or photochemical decay. Moreover, at that time the reactant and product populations on V_2 have converged to the same value ($\sim$0.10), i.e., the wave packet has spread over φ on V_2 because of the flat energy profile along that coordinate. This implies that any control scheme must achieve the selectivity in the early stages of the dynamics, before the wave packet spreads on V_2 and the selectivity is lost.

Our discussion is based on the adiabatic populations (see Eq. (10)). For comparison, in Figure 7(c) we show the reactant and product populations for the diabatic states. The differences are remarkable. For instance, the total population transferred to the ground state after 150 fs is 63% in the diabatic basis, compared to 81% in the adiabatic one. The adiabatic populations require an additional computational step and most publications therefore discuss only diabatic ones. However, given the substantial differences, we prefer to concentrate on the more physical adiabatic populations and will discuss only those in the following.

Overall, the results of the instantaneous excitation propagation are different from those described with previous approaches, where no double bond twist is observed after instantaneous vertical excitation of the wave packet. In the case of Ref. 26, where a three-dimensional model was used, the difference is probably be due to the different choice of the totally symmetric coordinate. In the present model, this mode (Q_{x_1}) contains a C_1–C_6 bond stretch component that is necessary for a good description of the surface, as seen from the changes in that distance along the relaxation coordinate (see Figure 2). Regarding Ref. 20, the different results obtained with the reduced dimensionality and the direct quantum dynamics approaches must be due to the different ways in which the IVR from the stretching to the torsional mode is treated, since both approaches use a similar electronic structure method for the potential. Regarding IVR, our reduced dimensionality propagations have two advantages: first, the dynamics is well converged (see Sec. III), and second, our curvilinear coordinates φ and θ are well adapted to the present problem. One may still question the fact that our model includes only four degrees of freedom. Although these are certainly the most relevant coordinates, inclusion of more degrees of freedom may slow down the IVR to the torsional mode, and this may account, in part, for the difference with respect to the direct dynamics approach. This issue will be addressed in future studies. On the other hand, the direct dynamics vMCG approach of Ref. 20 accounts for the full dimensionality of the problem but suffers from more approximate dynamics.

B. Pulse induced propagations

To approach experimental conditions, we have carried out propagations initiated with a single laser pulse. We have used pulses of 5 fs or 25 fs duration, and excitation energies
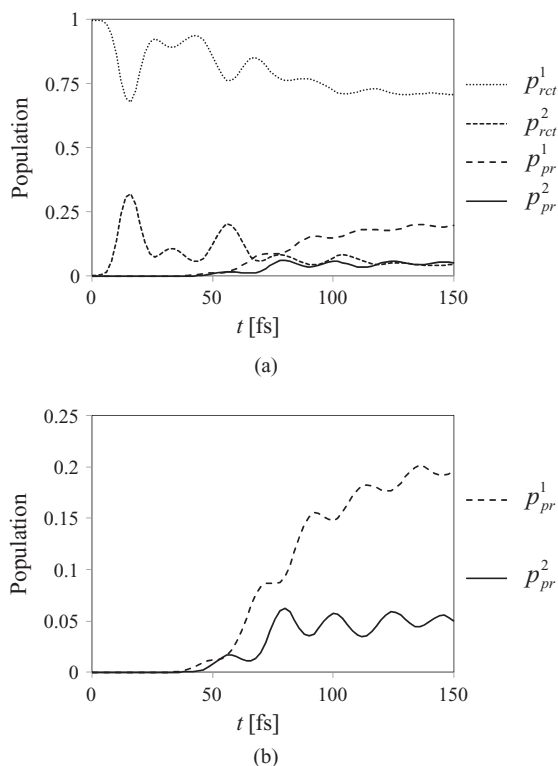
FIG. 8. (a) Reactant and product adiabatic populations for the two states after excitation with a pulse of 25 fs and 3.0 eV (see Eq. (9)). p_{rct}^1 (dotted line); p_{rct}^2 (short hashed line); p_{pr}^1 (long hashed line); p_{pr}^2 (continuous line). (b) Detailed plot of p_{pr}^1 and p_{pr}^2.
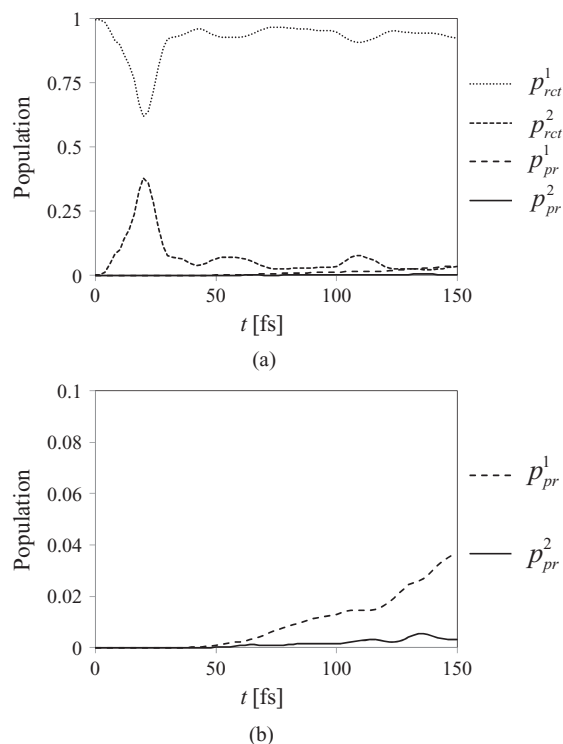
FIG. 9. (a) Reactant and product adiabatic populations for the two states after excitation with a pulse of 25 fs and 2.0 eV (see Eq. (9)). p_{rct}^1 (dotted line); p_{rct}^2 (short hashed line); p_{pr}^1 (long hashed line); p_{pr}^2 (continuous line). (b) Detailed plot of p_{pr}^1 and p_{pr}^2.

between 1.85 eV and 4.0 eV. Table II shows a summary of the propagation results. The competition between unreactive decay and isomerization to the product is monitored by determining the time required for 1% of product population to appear, which corresponds to the minimal time required for IVR from Q_{x_1} to φ, τ_{IVR}. This value is comparable between the different runs because the amount of population transferred to the excited state during the pulse is similar for all runs. This is monitored with the help of P_{max}^2, the maximum value of the adiabatic excited state population during the propagation, which ranges from 0.23 to 0.43 (see Table II).

First we describe a representative propagation initiated with a pulse of 25 fs and 3.0 eV energy (Figure 8). During the pulse, the population on V_2 starts to build up and p_{pr}^2 reaches a maximum value of 0.31 (P_{max}^2). After that, the propagation is similar to the vertical excitation case. Thus, a substantial amount of population is rapidly transferred back to V_1, and after 150 fs the excited state population is reduced to approximately one third of P_{max}^2 ($P_f^2 = 0.10$). Turning to the selectivity, the product configuration is only populated after ~40 fs, which corresponds to τ_{IVR}. At that time, a large amount of population has already been transferred back from the excited to the ground state. As soon as the product population appears on V_2, it also builds up on V_1, similar to the vertical excitation case. At the end of the propagation, the population of product on the ground state is 0.20. In turn, p_{rct}^2 and p_{pr}^2 are approximately equal, i.e., the wave packet has spread along φ on V_2. Excitation with energies between 2.5 eV and 4.0 eV produces similar results to the ones described for the 3.0 eV

pulse. The maximal amount of population transfer to V_2 is observed at 3.0 eV excitation energy, which is also the closest energy value to the vertical excitation energy from the **FC** structure in the model (3.2 eV).

Turning to the selectivity, the results for the runs with a 25 fs excitation pulse show that τ_{IVR} becomes shorter as the excitation energy increases. This trend implies that IVR from Q_{x_1} to φ is accelerated when the amount of excess energy along Q_{x_1} increases. More importantly, the increase in τ_{IVR} becomes more pronounced as the excitation energy approaches the 0–0 limit ($\hbar\omega \leq 2.0$ eV). As a consequence, the isomerization is almost completely suppressed at low excitation energies because it cannot compete with the decay near **CI$_{plan}$**, which is very efficient at all wave lengths. Such behavior is exemplified in Figure 9 for a run initiated by a 25 fs pulse of 2.0 eV excitation energy. During the propagation the wave packet is confined almost exclusively to the region around the initial value of φ, and the total product population hardly reaches 0.04. The dependence of τ_{IVR} on the excitation energy is also observed for the propagations initiated by short 5 fs pulses, although τ_{IVR} is somewhat shorter compared to the 25 fs pulse for the same excitation energy. In contrast to this, the efficiency of the population transfer from the excited to the ground state does not depend so critically on the excitation energy (compare the values of P_f^2 in Table II and Figures 8(a) and 9(a)). This is probably due to the fact that the barrier to reach **CI$_{Plan}$** from **(S$_1$)$_{Min}$** is only 0.2 eV on our model surface (0.3 eV on the reference *ab initio* surface, see Table I). With such a small barrier, even the

propagations started close to the 0–0 transition (1.85 eV) show a very fast population decay (shorter than 10 fs). This differs from the results described using the vMCG approach on a full dimensional surface. In that case, propagation of a wave packet set initially in the region of $(S_1)_{Min}$ induces a damped decay. The population transfer to the ground state is slowed down to about 70 fs, leaving time for the isomerization.

V. CONCLUSIONS

We have presented a four-dimensional model for the photodynamics of fulvene to model the competition between unreactive return to the ground state and double bond isomerization. The photoreactivity depends on a seam of conical intersection along a torsional and a pyramidalization coordinate, and our model reproduces the energies and locus of the seam along these coordinates and the branching space vectors associated to the seam. The model involves several approximations concerning the KEO, the number of modes, and the level of theory for the electronic structure calculations, but wave packet propagations on this model have allowed us to determine the principal characteristics of the early stage of the photodynamics. Initially, the excitation energy is transferred to a bond stretching mode that leads the wave packet straight to a region of conical intersection around planar or quasi-planar nuclear configurations, and this leads to regeneration of the reactant. The photoisomerization only takes place after some energy flows from the bond stretching to the torsional mode, and therefore the competition between unreactive decay and isomerization depends on the rate of IVR between these two coordinates. In our propagations, IVR is accelerated for higher excess energies along the bond stretch mode. Thus, when the excitation energy is sufficiently high (2.5 eV or more in the present case, which is ∼0.6 eV above the 0–0 transition energy), IVR takes less than 50 fs and the photoisomerization competes with the unreactive decay. In contrast to this, for excitation energies near the 0–0 threshold (2.0 eV or less) IVR is slowed down by up to a factor of three, and the isomerization is virtually suppressed. Given the importance of IVR in the outcome of the decay, in future work we will inspect if the relationship between IVR and excitation energy that we have observed here is preserved when more degrees of freedom are included in the model.

From a general point of view, the photodynamics of fulvene can be described as a two-step, two-mode process. Initially the excitation energy flows into the first mode, which leads to the unreactive decay region of the seam. If IVR is sufficiently fast, decay along the second mode can take place, which leads to the reactive region of the seam. This feature is quite general for photochemical processes. For example, in the polyenes used to model the photoisomerization of retinal, the chromophore of rhodopsin proteins,[39] the first mode is a bond inversion mode of the polyene chain, and the second mode the cis-trans isomerization coordinate (double bond rotation).[40] In benzene, the first mode is a bond stretching coordinate of the ring, and the second one a ring puckering mode (strictly speaking, a combination of two out-of-plane normal modes) that leads to formation of a prefulvene product (channel 3 of benzene).[18] In both cases, the photochemical event requires IVR from the first to the second mode. Based on our results, it will be interesting to investigate these processes focusing on how IVR affects the product formation rate and how this depends on the excitation energy.

Turning to our aim of controlling the photoreactivity, we can compare the present results with our previous MCTDH studies on intramolecular energy redistribution in molecules in their electronic ground state (Chapter 21 in Ref. 2). The basis of this approach was to create specific wave packets as linear combinations of converged vibrational eigenstates. In addition to the propagations initiated by single pulses we have tried a similar approach to control the photodynamics of fulvene, but due to the enormous density of states it has not been possible to converge any eigenstates in the vicinity of the conical intersection. Therefore, control of chemical processes involving conical intersections seems to be a much more difficult task. In such a context, the present work highlights the role of IVR in the photodynamics, and it suggests that controlling IVR will be necessary to control the photoreactivity.

[1] A. H. Zewail, in *Femtochemistry*, edited by F. C. De Schryver, S. De Feyter, and G. Schweitzer (Wiley VCH, Weinheim, Germany, 2001), pp. 1–86.

[2] H.-D. Meyer, F. Gatti, and G. A. Worth, *Multidimensional Quantum Dynamics: MCTDH Theory and Applications* (Wiley VCH, Weinheim, Germany, 2009).

[3] H. D. Meyer, U. Manthe, and L. S. Cederbaum, Chem. Phys. Lett. **165**, 73 (1990).

[4] M. H. Beck, A. Jackle, G. A. Worth, and H. D. Meyer, Phys. Rep. **324**, 1 (2000).

[5] F. Richter, M. Hochlaf, P. Rosmus, F. Gatti, and H. D. Meyer, J. Chem. Phys. **120**, 1306 (2004).

[6] F. Richter, P. Rosmus, F. Gatti, and H. D. Meyer, J. Chem. Phys. **120**, 6072 (2004).

[7] F. Richter, F. Gatti, C. Leonard, F. Le Quere, and H. D. Meyer, J. Chem. Phys. **127**, 164315 (2007).

[8] R. Marquardt, M. Sanrey, F. Gatti, and F. Le Quere, J. Chem. Phys. **133**, 174302 (2010).

[9] G. J. Atchity, S. S. Xantheas, and K. Ruedenberg, J. Chem. Phys. **95**, 1862 (1991).

[10] M. J. Bearpark, F. Bernardi, M. Olivucci, M. A. Robb, and B. R. Smith, J. Am. Chem. Soc. **118**, 5254 (1996).

[11] L. Blancafort, F. Ogliaro, M. Olivucci, M. A. Robb, M. J. Bearpark, and A. Sinicropi, in *Computational Methods in Photochemistry*, edited by A. G. Kutateladze (Taylor & Francis, Boca Raton, FL, 2005), vol. 13, pp. 31–110.

[12] M. Klessinger and J. Michl, *Excited States and Photochemistry of Organic Molecules* (VCH Publishers, Inc., New York, 1995).

[13] D. R. Yarkony, J. Phys. Chem. A **105**, 6277 (2001).

[14] L. Blancafort, B. Lasorne, M. J. Bearpark, G. A. Worth, and M. A. Robb, in *The Jahn-Teller Effect: Fundamentals and Implications for Physics and Chemistry*, edited by H. Köppel, D. R. Yarkony, and H. Barentzen (Springer, Heidelberg/Berlin, 2009), pp. 169–200.

[15] M. Araujo, B. Lasorne, A. L. Magalhaes, M. Bearpark, and M. A. Robb, J. Phys. Chem. A **114**, 12016 (2010).

[16]D. Asturiol, B. Lasorne, G. A. Worth, M. A. Robb, and L. Blancafort, Phys. Chem. Chem. Phys. **12**, 4949 (2010).

[17]M. Kobylecka, A. Migani, D. Asturiol, J. Rak, and L. Blancafort, J. Phys. Chem. A **113**, 5489 (2009).

[18]B. Lasorne, M. J. Bearpark, M. A. Robb, and G. A. Worth, J. Phys. Chem. A **112**, 13017 (2008).

[19]A. Migani, L. Blancafort, A. D. DeBellis, and M. A. Robb, J. Am. Chem. Soc. **130**, 6932 (2008).

[20]D. Mendive-Tapia, B. Lasorne, G. A. Worth, M. J. Bearpark, and M. A. Robb, Phys. Chem. Chem. Phys. **12**, 15725 (2010).

[21]K. R. Asmis, M. Allan, O. Schafer, and M. Fulscher, J. Phys. Chem. A **101**, 2089 (1997).

[22]P. J. Domaille, J. E. Kent, and M. F. Odwyer, Chem. Phys. **6**, 66 (1974).

[23]J. E. Kent, P. J. Harman, and M. F. Odwyer, J. Phys. Chem. **85**, 2726 (1981).

[24]F. Sicilia, M. J. Bearpark, L. Blancafort, and M. A. Robb, Theor. Chem. Acc. **118**, 241 (2007).

[25]S. Alfalah, S. Belz, O. Deeb, M. Leibscher, J. Manz, and S. Zilberg, J. Chem. Phys. **130**, 124318 (2009).

[26]S. Belz, T. Grohmann, and M. Leibscher, J. Chem. Phys. **131**, 034305 (2009).

[27]O. Deeb, M. Leibscher, J. Manz, W. von Muellern, and T. Seideman, ChemPhysChem **8**, 322 (2007).

[28]G. A. Worth, M. H. Beck, A. Jackle, and H. D. Meyer, The MCTDH Package, Version 8.2, University of Heidelberg, Heidelberg, Germany, 2000;

H.-D. Meyer, The MCTDH Package, Version 8.3, 2002 and Version 8.4, 2007; see http://mctdh.uni-hd.de.

[29]M. J. Frisch, G. W. Trucks, H. B. Schlegel *et al.*, GAUSSIAN 03, Revision B.02, Gaussian, Inc., Pittsburgh, PA, 2003.

[30]G. Karlstrom, R. Lindh, P. A. Malmqvist, B. O. Roos, U. Ryde, V. Veryazov, P. O. Widmark, M. Cossi, B. Schimmelpfennig, P. Neogrady, and L. Seijo, Comput. Mater. Sci. **28**, 222 (2003).

[31]B. O. Roos, and K. Andersson, Chem. Phys. Lett. **245**, 215 (1995).

[32]G. Ghigo, B. O. Roos, and P. Å. Malmqvist, Chem. Phys. Lett. **396**, 142 (2004).

[33]H. Köppel, W. Domcke, and L. S. Cederbaum, Adv. Chem. Phys. **57**, 59 (1984).

[34]H. Köppel, J. Gronki, and S. Mahapatra, J. Chem. Phys. **115**, 2377 (2001).

[35]F. Gatti and C. Iung, Phys. Rep. **484**, 1 (2009).

[36]M. R. Brill, F. Gatti, D. Lauvergnat, and H. D. Meyer, Chem. Phys. **338**, 186 (2007).

[37]A. Jäckle and H. D. Meyer, J. Chem. Phys. **104**, 7974 (1996).

[38]A. Jäckle and H. D. Meyer, J. Chem. Phys. **109**, 3772 (1998).

[39]Y. Shichida and T. Yoshizawa, in *CRC Handbook of Organic Photochemistry and Photobiology*, 2nd ed., edited by W. Horspool and F. Lenci (CRC, Boca Raton (FL), 2004), vol. 2.

[40]M. Olivucci, A. Lami, and F. Santoro, Angew. Chem. Int. Ed. **44**, 5118 (2005).